

Numerical simulation study of a high efficient AlGaIn-based ultraviolet photodetector

F. Bouzid^{1,2,*}, L. Dehimi^{3,4}, F. Pezzimenti⁵, M. Hadjab^{1,2}, A. Hadj Larbi^{1,2}

¹Research Center in Industrial Technologies CRTI, P.O. Box 64, Cheraga 16014, Algiers, ALGERIA.

²Thin Films Development and Applications Unit UDCMA, Setif 19000, ALGERIA.

³Laboratory of Metallic and Semiconductor Materials, University of Biskra, P.B.145, Biskra-ALGERIA.

⁴Batna University, Physics Department, Batna-ALGERIA.

⁵DIIES - University of Reggio Calabria, Loc. Feo di Vito, Reggio Calabria 89100, ITALY.

*E-mail: f.bouzid@crti.dz

Abstract

In this paper, a two-dimensional (2D) numerical simulation study of a p⁺-n-n⁺ AlGaIn-based ultraviolet (UV) photodetector, which is designed to achieve true solar blindness with a cutoff wavelength of 0.31 μm, is presented. The device performance is evaluated by investigating both the current density-voltage characteristics and the spectral response (SR). The proposed structure is optimized in terms of the fundamental geometrical and doping parameters. During the simulations, it was found that the detector is sensitive to the UV rays in the 0.155-0.37 μm wavelength range and the spectral response can reach 0.156 AW⁻¹ under a light intensity of 1 Wcm⁻² at zero-bias voltage and room temperature. This SR peak value increases further under reverse bias conditions. The temperature effect on the detector SR and the impact of an explicit trap concentration located into the p⁺ and n region are also investigated. The spectral response decreases for a temperature exceeding 420 K. At the same time, the SR reference values begin to be affected only for acceptor and donor trap densities that are much higher than the local (total) doping concentration.

Keywords: AlGaIn, Numerical Simulation, Photodetector, Spectral Response, Trap Density.

1. Introduction

Semiconductor-based radiation detectors have been developed for several applications in various fields, which involve, for example, industrial and medical sectors as well as astrophysics, control, and environment.

Gallium Nitride (GaN) is one of the most interesting semiconductor compounds well suited to be used in any application in which the temperature and/or level of radiation could damage conventional silicon (Si) or gallium arsenide (GaAs) electronics [1]. Compared with other materials, the most attractive properties of GaN are the wide bandgap (3.4 eV), high saturation velocity, high thermal conductivity, strong breakdown electric field, and ability to form high quality heterostructures with good transport properties [2]. In recent years, a large number of GaN-based devices have been developed, such as light-emitting diodes, laser diodes, photodetectors, and particle detectors [3-7]. In addition, the detection of ultraviolet (UV) radiation by means of GaN devices has gained a great interest in many important areas requiring high performance photodetectors, low dark current, and high sensitivity as, for example, optical space communications, reactor monitoring, missile detection, flame detection, detection of biological and chemical agents, ozone layer monitoring and quantum optics [8-11]. Different types of GaN and Al_xGa_{1-x}N compounds-based photodetection structures have been studied, namely simple PN junctions [12,13], PIN structures [14-16], metal-semiconductor-metal structures [17-19], AlGaIn/GaN and InGaIn/GaN heterojunctions [20,21], and Schottky structures [22,23].

In the last decade, in particular, AlGaIn-based p⁺-n-n⁺ UV photodetectors have been extensively proposed [24-36]. In most of these photodetectors, the light must pass through a so called "window" layer before reaching the absorbing layer (n-region). These photodetectors often operate under a low

reverse bias with a relatively constant electric field across the entire n-AlGa_xN layer where a space charge region is formed [36]. From the literature data, the performance of several p⁺-n-n⁺ UV-light detectors based on the Al_xGa_{1-x}N ternary compound is summarized in Table 1.

Table 1. Performance of several p⁺-n-n⁺ photodetectors at room temperature.

p	i	n	Lightening	λ_{pic} (nm)	$\lambda_{cut-off}$ (nm)	SR peak at 0V (AW ⁻¹)	Ref.
GaN	Al _{0.17} Ga _{0.83} N	GaN	Front	350	375	0.114(-15V)	[24]
GaN	Al _{0.17} Ga _{0.83} N	GaN	Back	350	375	0.067(-15V)	[24]
GaN	Al _{0.33} Ga _{0.67} N	GaN	Front	287	360	0.057	[25]
GaN	Al _{0.44} Ga _{0.56} N	Al _{0.44} Ga _{0.56} N	Front	270	365	0.12	[26]
GaN	Al _{0.30} Ga _{0.70} N	Al _x Ga _{1-x} N (x > 0.30)	Back	285	350	0.08	[27]
Al _{0.40} Ga _{0.60} N	Al _{0.40} Ga _{0.60} N	Al _{0.40} Ga _{0.60} N	Back	278	289	-	[28]
Al _{0.47} Ga _{0.53} N	Al _{0.39} Ga _{0.61} N	Al _{0.47} Ga _{0.53} N	Back	279	291	0.058 0.07 (-5V)	[29]
Al _{0.48} Ga _{0.52} N	Al _{0.48} Ga _{0.52} N	Al _{0.57} Ga _{0.43} N	Back	269	279	0.09 0.11 (-5V)	[30]
Al _{0.46} Ga _{0.54} N	Al _{0.46} Ga _{0.54} N	Al _{0.54} Ga _{0.46} N	Back	272	280	-	[31]
Al _{0.38} Ga _{0.62} N	Al _{0.40} Ga _{0.60} N	Al _{0.45} Ga _{0.55} N	Back	279	285	0.0862 0.129 (-40V)	[32]
P ⁺ -SiC	AlN/i-SiC	Al _{0.80} Ga _{0.20} N	Front	242	260	0.15(-40V)	[33]
Al _{0.38} Ga _{0.62} N	Al _{0.40} Ga _{0.60} N	Al _{0.45} Ga _{0.55} N	Back	278	285	0.109	[34]
Al _{0.45} Ga _{0.55} N	Al _{0.45} Ga _{0.55} N	Al _{0.55} Ga _{0.45} N	Back	269	281	0.12 0.149(-5V)	[35]

In this work, we investigated a high responsivity p⁺-n-n⁺ Al_xGa_{1-x}N UV photodetector for frontal lighting where an aluminum (Al) molar fraction $x = 0.17$ was fixed to obtain a bandgap energy of 3.99 eV at room temperature. This value was calculated by using [37]

$$E_g(x, T) = xE_g^{AlN}(T) + (1 - x)E_g^{GaN}(T) - 0.6x(1 - x) \quad (1)$$

where $E_g^{AlN}(T)$ and $E_g^{GaN}(T)$ are temperature-dependent constants [37]. More in detail, a two-dimensional (2D) numerical analysis was developed by means of the physical device simulator Atlas-Silvaco [38] solving the Poisson's equation and the carrier continuity equations. The thickness and doping concentration of the p⁺-region were carefully optimized. The effect of different radiation wavelengths on the device current capabilities, as well as the temperature effect and the impact of an explicit trap density in both the device p⁺ and the n regions on its spectral response (SR) were also evaluated. The detector SR can reach 0.156 AW⁻¹ under a light intensity of 1 Wcm⁻² at zero-bias voltage and room temperature. This SR peak value increases further under reverse bias conditions. The detector cut-off wavelength is 0.31 μ m, which guarantees a true solar blindness.

2. Device structure and parameters

The schematic cross section of the proposed Al_{0.17}Ga_{0.83}N UV photodetector is shown in Fig. 1. The simulated footprint area is 12 μ m². The electrodes on the top and bottom of the device are both ohmic contacts. In particular, the Ti/Al alloy, which is commonly used for GaN n-doped layers, is assumed as cathode on the whole back surface. Platinum (Pt) with a work function of 5.65 eV [39] forms the anode contact. Recently, in fact, it was experimentally highlighted that p-type AlGa_xN samples with Pt as contact may exhibit a good ohmic behavior [39,40].

The Pt contact thickness is 5 nm and its length is 2.9 μm . These geometrical parameters were fixed after several attempts. In particular, the simulations under illumination reveal that an anode thickness higher than 6 nm marks the set up of a significant decrease of both the carrier photogeneration and the detector spectral responsivity. Devices with Pt contact thicknesses close to 5 nm were characterized, for example, in [41,42].

The p^+ layer below the anode contact is 0.1 μm thick with a doping concentration of $1 \times 10^{16} \text{ cm}^{-3}$. The n-type intrinsic region has a thickness of 0.2 μm and a doping concentration of $1 \times 10^{13} \text{ cm}^{-3}$. The main disadvantage of the p^+ -n- n^+ AlGaIn-based detectors is the difficulty of forming high quality ohmic contacts [8]. To overcome this problem, a highly doped thin layer of GaN below the n^+ region is put in contact with the metal. For this reason, in the device structure in Fig. 1 we can see a 0.8 μm -thick and $5 \times 10^{17} \text{ cm}^{-3}$ -doped n^+ -layer, and also a 0.2 μm -thick and $8 \times 10^{19} \text{ cm}^{-3}$ -doped n^+ -type GaN layer at the cathode contact interface.

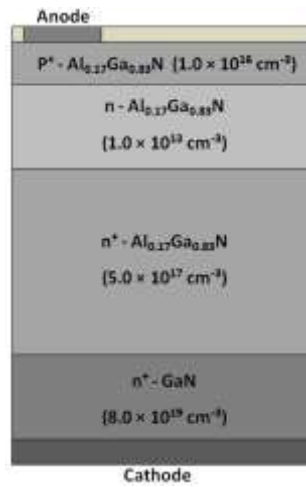


Fig. 1. $\text{Al}_{0.17}\text{Ga}_{0.83}\text{N}$ UV photodetector schematic cross section. The drawing is not in scale.

The presented device structure was modeled and finely meshed wherever appropriate during the simulations, in particular into the p^+ region and at the p^+/n and n/n^+ interfaces. The fundamental simulation parameters assumed at room temperature are listed in Table 2.

Table 2. Physical model parameters assumed at $T = 300 \text{ K}$.

Parameters	GaN	AlGaIn
E_g (eV)	3.4	3.99
ϵ_r	9.5	9.2
τ_n (s)	10^{-9}	10^{-10}
τ_p (s)	10^{-9}	10^{-10}
v_{sat} (cms ⁻¹)	0.95×10^7	1.5×10^7
χ (eV)	4.1	4.02
N_c (cm ⁻³)	2.65×10^{18}	3.09×10^{18}
N_v (cm ⁻³)	2.5×10^{19}	1.03×10^{20}

Here, E_g is the temperature dependent bandgap energy, ϵ_r is the material permittivity, τ_n and τ_p are the carrier lifetimes, v_{sat} is the carrier saturation velocity, χ is the electron affinity, and N_c and N_v are the electron and hole density of states varying with temperature. The simulation setup adopted in this work has been also used in other recent papers of ours where the relative physical models are described in detail [43-47].

2. 1 p⁺-Region doping

To find out the optimal acceptor doping concentration N_a of the p⁺-region, which corresponds to the best detector performance in terms of SR, we performed several simulations for N_a in the range $1 \times 10^{15} - 1 \times 10^{17} \text{ cm}^{-3}$. The obtained results at zero-bias voltage are shown in Fig. 2.

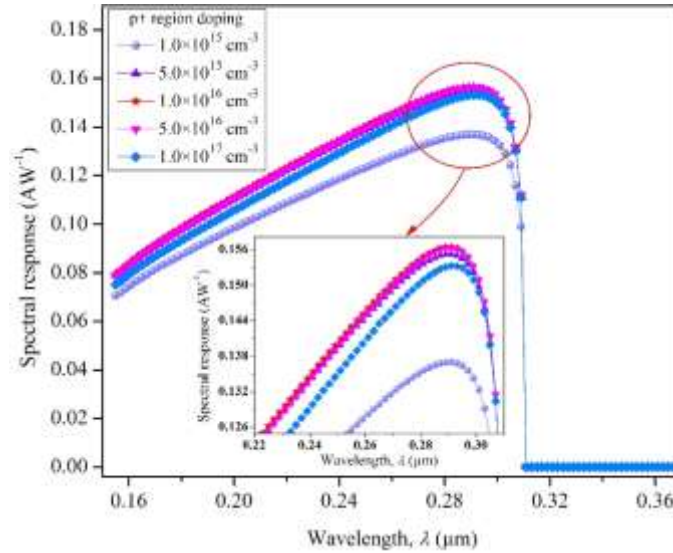
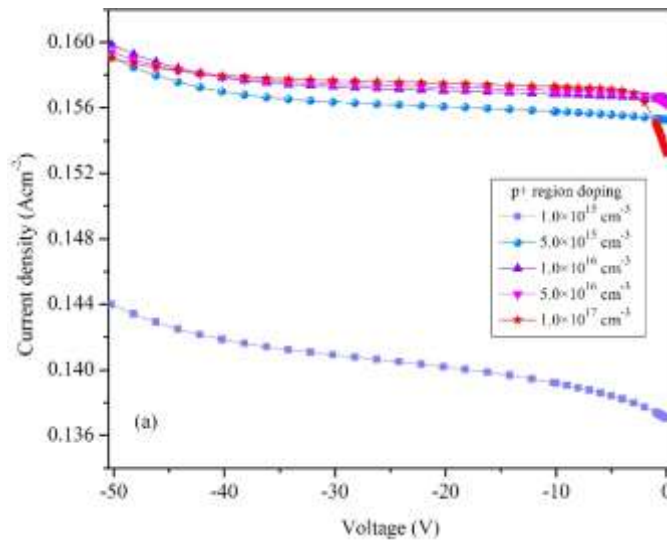


Fig. 2. SR as a function of the doping concentrations in the p⁺-region under a light intensity of 1 Wcm^{-2} at zero-bias voltage and $T = 300 \text{ K}$.

From Fig. 2, the spectral response increases progressively with increasing the doping concentration up to $N_a = 1 \times 10^{16} \text{ cm}^{-3}$. It reaches a maximum value of 0.156 AW^{-1} and then begins to decrease gradually and becomes 0.153 AW^{-1} for $N_a = 1 \times 10^{17} \text{ cm}^{-3}$. This SR behavior can be explained considering the different thickness of the depletion region with respect to the increase of the doping concentration. In particular, as it is well known, the photogenerated carriers in the depletion region are swept out by the built-in electric field that increases with increasing the concentration of acceptor atoms in the emitter region. However, at higher doping levels, a decrease of the carrier diffusion length determines an overall decreasing of the photodetector output current as highlighted in Fig. 3 (a).



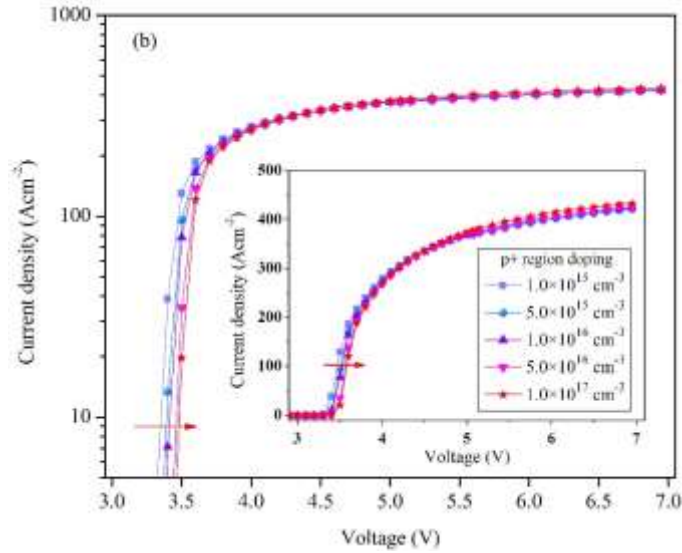


Fig. 3. $J(V)$ characteristics for different doping concentrations of the p^+ -region under a light intensity of 1 Wcm^{-2} at $T = 300 \text{ K}$. (a) Reverse bias. (b) Forward bias.

An increase in the reverse current is observed with increasing the doping concentration of the p^+ -region at low reverse biases. Then, a lowering of the curves occurs when the doping concentration exceeds the value of $1 \times 10^{16} \text{ cm}^{-3}$. In addition, by simulating the forward $J(V)$ curves as shown in Fig. 3 (b), the device threshold voltage increases slightly with increasing N_a . This current behavior is mainly due to the increase of the voltage drop across the n -region.

2. 2 p^+ -Region thickness

In the $p^+ - n - n^+$ photodetectors, the n -region represents the most efficient location for absorption. However, since the depletion region extends into the p^+ -region, the thickness of both the p^+ and n region affects the SR value. The detector SR as a function of the p^+ -region thickness at zero-bias voltage and $T = 300 \text{ K}$ is shown in Fig. 4.

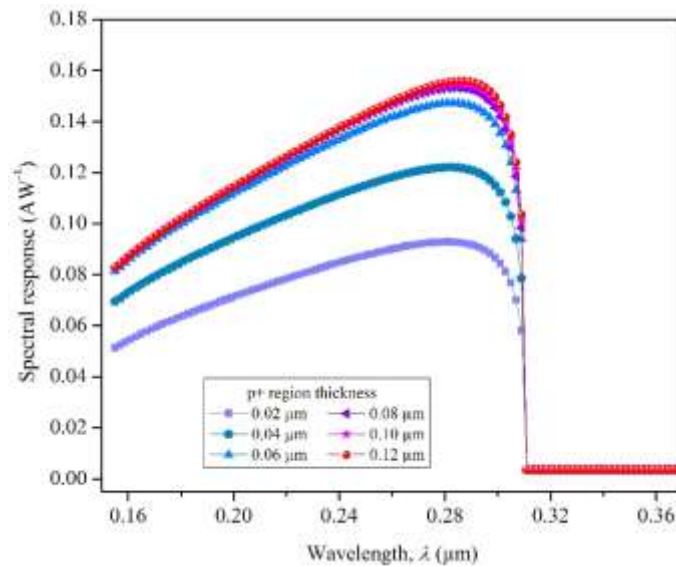


Fig. 4. SR as a function of the p^+ -region thickness under a light intensity of 1 Wcm^{-2} at zero-bias voltage and $T = 300 \text{ K}$.

It can be seen that the spectral response behavior increases significantly with increasing the p^+ -region thickness from $0.02 \mu\text{m}$ to $0.08 \mu\text{m}$ and the relative SR peak increases from 0.092 AW^{-1} to 0.153 AW^{-1} , respectively. However, when the p^+ -region thickness exceeds $0.08 \mu\text{m}$ this effect is poor and the SR peak stabilizes at a value close to 0.156 AW^{-1} for a thickness of $0.1 \mu\text{m}$. It is worthwhile noting that the p^+ -region thickness increase makes it possible to absorb more incident photons that lead to an increase in the photocurrent as shown in Fig. 5 (a) for reverse bias conditions. On the other hand, the SR behavior tends to stabilize for a proper thickness value (i.e., $0.1 \mu\text{m}$ in this case) when the curve is mainly determined by the recombination phenomena.

Finally, it is noted that the forward $J(V)$ characteristics are substantially unchanged for different values of the p^+ -region thickness as shown in Fig. 5 (b).

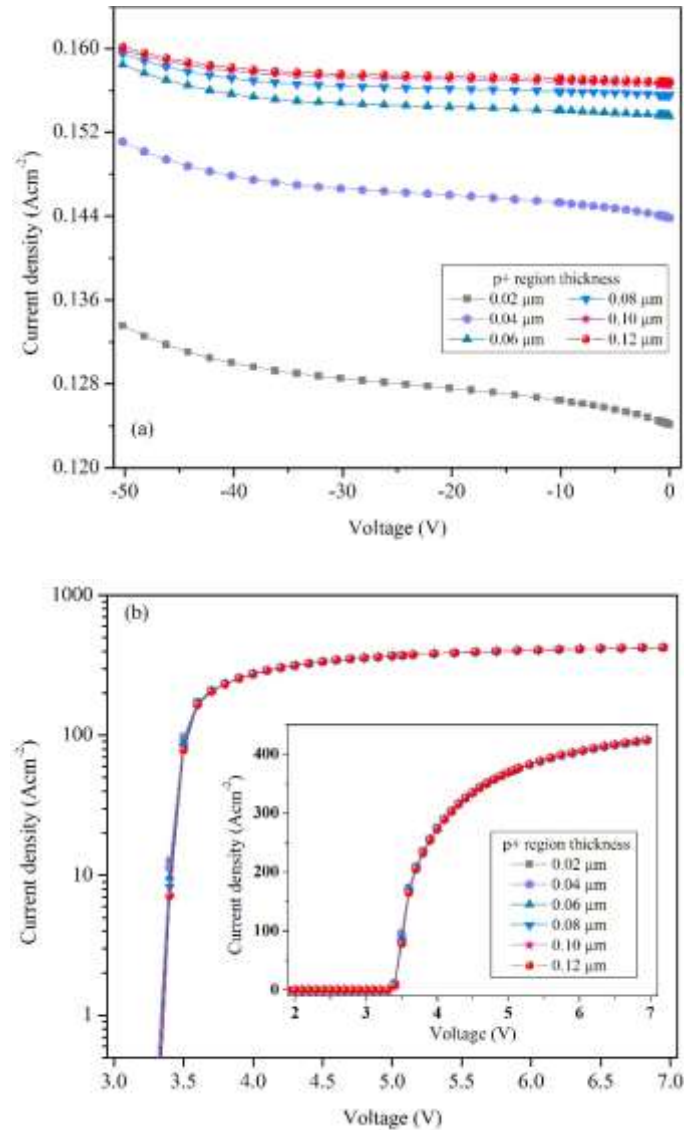


Fig. 5. $J(V)$ characteristics for different thicknesses of the p^+ -region under a light intensity of 1 Wcm^{-2} at $T = 300 \text{ K}$. (a) Reverse bias. (b) Forward bias.

2.3 n-Region thickness

The number of absorbed photons is related to the depletion region width w and absorption coefficient α which depends on the wavelength. If the reflection on the surface of the illuminated photodetector is neglected, the spectral response can be expressed as [35]:

$$SR(\lambda) = 1 - \exp[-\alpha(\lambda)w] \quad . \quad (2)$$

In order to improve the spectral response, the depletion region width, which mainly lies in the intrinsic region, should be rather wide. The SR behavior as a function of the n-region thickness at zero-bias voltage and $T=300$ K is shown in Fig. 6. Here, in accordance with (2), it is evident that SR increases with an increasing thickness of the n-region as clearly shown in the inset (zoom-in view).

Theoretically, if the width of the depletion region is wide enough, the spectral response may reach the maximum value of 1. Practically, the typical width of the n-region is between $0.1 \mu\text{m}$ and $0.6 \mu\text{m}$ [35] considering that its increase origins some technological issues as the increased etching depth. In this work a $0.2 \mu\text{m}$ -thick n-region was assumed by default.

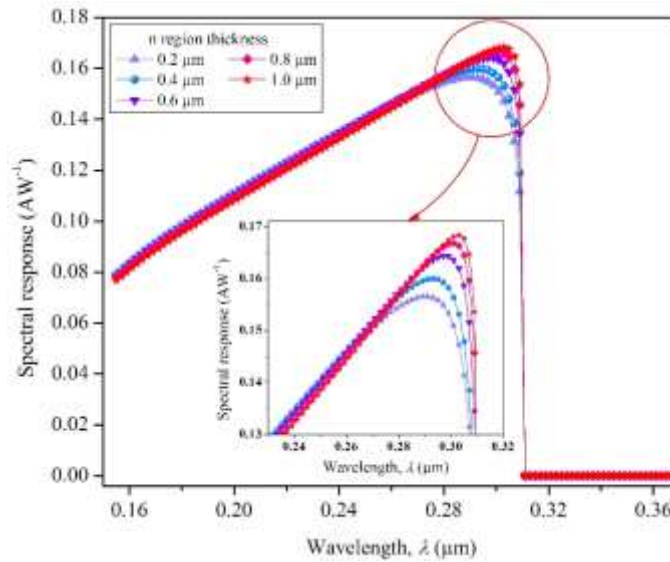


Fig. 6. SR as a function of the n-region thickness under a light intensity of 1 Wcm^{-2} at zero-bias voltage and $T = 300$ K.

3. Results and discussion

3.1 Effect of the incident radiation wavelength on the detector $J(V)$ characteristics

The detector current density-voltage characteristics as a function of different wavelengths of the incident radiation are shown in Fig. 7, both in the forward and reverse bias conditions.

The current density curves appear almost unchanged for forward biases. On the other hand, we can note different $J(V)$ behaviors for reverse biases. In particular, the reverse current increases with increasing the wavelength value as a consequence of the improvement of the photogeneration rate as reported in Fig. 8.

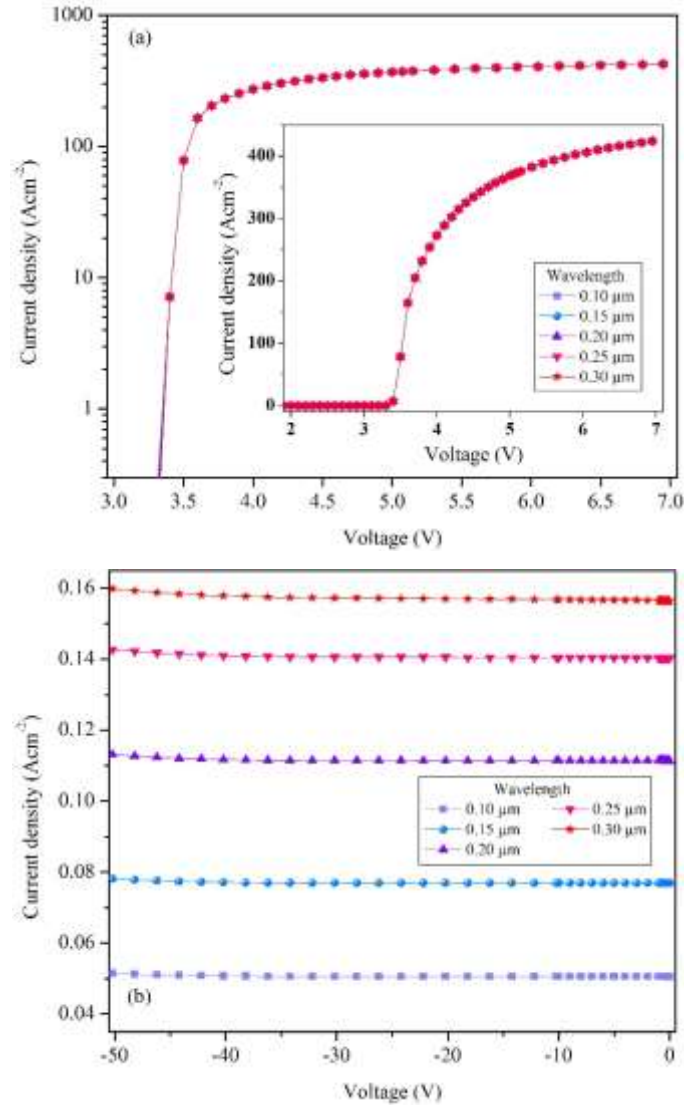


Fig. 7. $J(V)$ characteristics for different wavelengths of the incident radiation under a light intensity of 1 Wcm^{-2} at $T = 300 \text{ K}$. (a) Forward bias. (b) Reverse bias.

In the zoomed area (inset) of Fig. 8, it is found that the photogeneration rate decreases slightly near the detector anode surface with the increase of the incident radiation wavelength, while the opposite occurs in the bulk region. This phenomenon is mainly due to the large penetration depth of long wavelengths in the device structure, in contrast to the low wavelengths that are well absorbed for low thicknesses. These results show that the designed UV photodetector is in principle capable of acting as a light wavelength selector device.

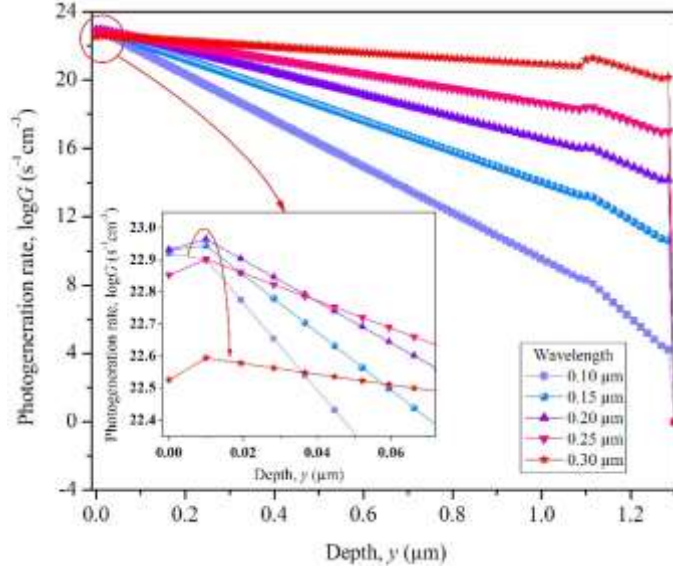


Fig. 8. Photogeneration rate profile across the detector for different wavelengths of the incident radiation under a light intensity of 1 Wcm^{-2} at $T = 300 \text{ K}$.

3. 2 Temperature and reverse-bias voltage effect

The detector SR behaviors for different temperatures ranging from 300 K to 500 K are shown in Fig. 9. The variation of the $\text{Al}_{0.17}\text{Ga}_{0.83}\text{N}$ absorption coefficient was assumed in the form of [35]:

$$\alpha(T) = 10^5 \sqrt{E - E_g(T)} \quad (3)$$

where E is the photon energy and $E_g(T)$ is the material bandgap.

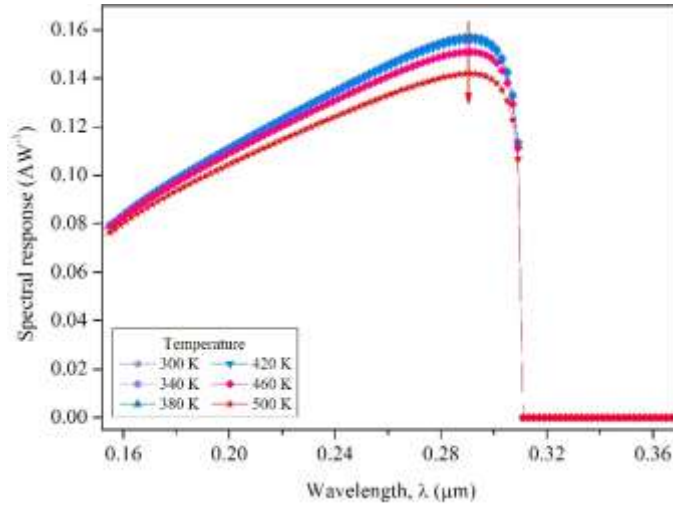


Fig. 9. SR as a function of the temperature under a light intensity of 1 Wcm^{-2} at zero-bias voltage.

The SR increases gradually with increasing wavelengths, for example from 0.079 AW^{-1} at $0.155 \text{ }\mu\text{m}$ to 0.156 AW^{-1} at $0.29 \text{ }\mu\text{m}$ ($T = 300 \text{ K}$), due to an increased penetration depth of the light. Then, it drops sharply at the cut-off wavelength of $0.31 \text{ }\mu\text{m}$. We can note that the temperature effect is quite limited for short wavelengths because most of the corresponding photons are absorbed. On the other hand, the temperature increase determines a decrease in the SR peak which is 0.141 AW^{-1} at $T = 500 \text{ K}$. This decrease, however, is noticeable only for $T \geq 420 \text{ K}$. At higher temperatures, in fact, the thermal agitation of the crystal lattice becomes more intense resulting in a reduction of the minority carriers mobility, lifetime, and diffusion coefficient. The recombination mechanisms become stronger and dominate the photogeneration phenomena that induce a reduction of the spectral response.

In order to partially compensate this detrimental effect of the temperature on the detector SR, a reverse-bias voltage could be applied to the device. In fact, from the simulations, an increased reverse-bias condition tends to improve the charge collection efficiency increasing the SR behavior. This result is shown in Fig. 10 at $T = 300 \text{ K}$.

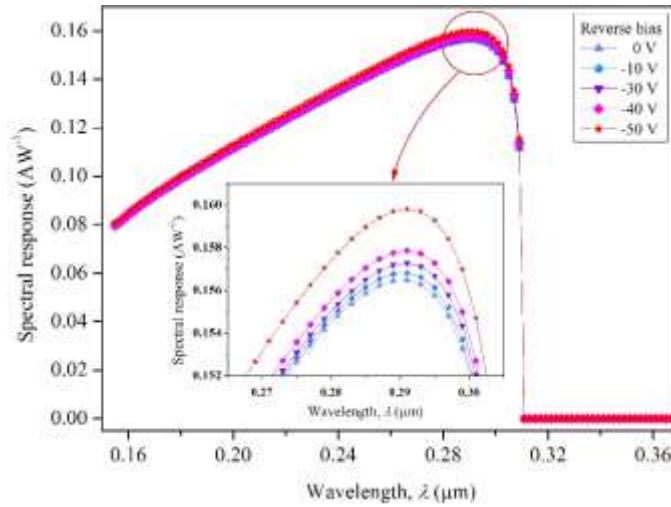


Fig. 10. SR for different reverse-bias voltages under a light intensity of 1 Wcm^{-2} at $T = 300 \text{ K}$. The inset shows a zoom-in view from $\lambda = 0.265 \text{ }\mu\text{m}$ to $\lambda = 0.305 \text{ }\mu\text{m}$.

The SR peak, which is 0.156 AW^{-1} for $\lambda = 0.29 \text{ }\mu\text{m}$ at zero-bias voltage, increases, for example, to 0.16 AW^{-1} for a reverse-bias voltage of -50 V . Similar SR behaviors were observed considering different temperatures of operation.

3.3 Effect of traps

The structural defects and the impurity atoms in III-N compounds give rise to a large variety of donor and acceptor states which can form complexes that trap charges of opposite types. Many researchers have worked on the identification of the main electron and hole defect centers in the bandgap of AlGaIn compounds, in terms of type, location, and origin by using different experimental methods, such as deep level transient spectroscopy (DLTS), Monte Carlo tree search (MCTS), and optical deep level transient spectroscopy (ODLTS). These studies have found that p-AlGaIn layers often contain a donor state located at 0.12 eV below the bottom of the conduction band (i.e., $E_c - 0.12 \text{ eV}$) created by the Mg-H complex and labeled as ET1. Magnesium (Mg), in fact, is the preferred p-type dopant to form p-GaN and p-AlGaIn regions. On the other hand, it has been shown that the interstitial impurities, namely

C, O, and H can form an acceptor state in the n-AlGaIn layers located at 0.44 eV above the top of the valence band (i.e., $E_v + 0.44$ eV) usually labeled HT1.

The fundamental trap parameters used during the simulations are summarized in Table 3.

Table 3. ET1 and HT1 trap parameters.

Type	Activation energy (eV)	Origin	Capture cross section (cm^2)	Ref.
ET1	0.12	Mg-H complex	1.0×10^{-18}	[48,49]
HT1	0.44	C,O,H impurity	4.0×10^{-21}	[50]

3.4.1 Donor trap ET1

By illuminating the detector in the 0.155-0.370 μm wavelength range with a light intensity of 1 Wcm^{-2} at zero-bias and $T = 300 \text{ K}$, the detector SR curves for a different donor trap concentration N_{td} located into the p^+ -region (ET1-type in Table 3) are shown in Fig. 11.

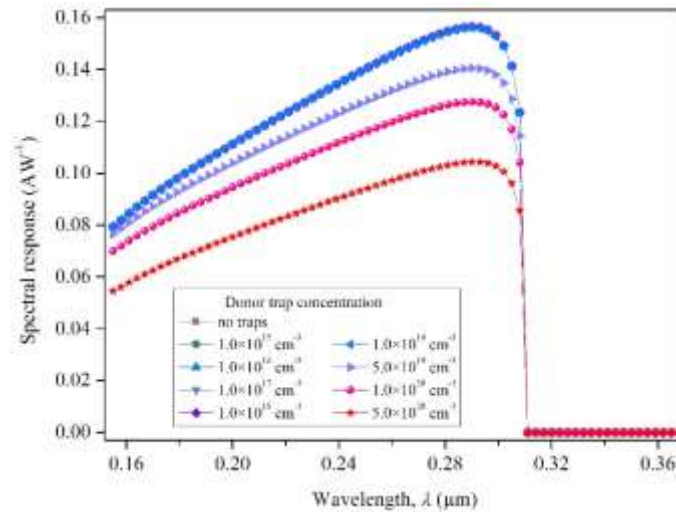


Fig. 11. SR for different concentrations of donor traps ET1 located into the p^+ -region. The light intensity is 1 Wcm^{-2} at zero-bias voltage and $T = 300 \text{ K}$.

Although we assumed N_{td} ranging from $1 \times 10^{15} \text{ cm}^{-3}$ to $5 \times 10^{20} \text{ cm}^{-3}$, the curves show that the detector SR is not affected by a trap concentration $N_{td} \leq 1 \times 10^{19} \text{ cm}^{-3}$, and a peak value close to 0.156 AW^{-1} at $0.29 \mu\text{m}$ can be calculated. On the other hand, when $N_{td} > 1 \times 10^{19} \text{ cm}^{-3}$ we observe a SR decrease in the whole explored wavelength range and the SR peak decreases to 0.1 AW^{-1} for $N_{td} = 5 \times 10^{20} \text{ cm}^{-3}$. The observed SR decrease, as soon as the donor trap density exceeds $1 \times 10^{19} \text{ cm}^{-3}$, is related to the carrier concentration profiles that origin along the device structure as shown in Fig. 12 for $\lambda = 0.29 \mu\text{m}$.

As we can see from Fig. 12 (a) the electron concentration in the p^+ -region (i.e., up to $y \leq 0.1 \mu\text{m}$) increases with increasing the donor trap density since they ionize and generate more electrons. At the same time, from Fig. 12 (b) the hole concentration decreases in this region as a result of an increased carrier recombination.

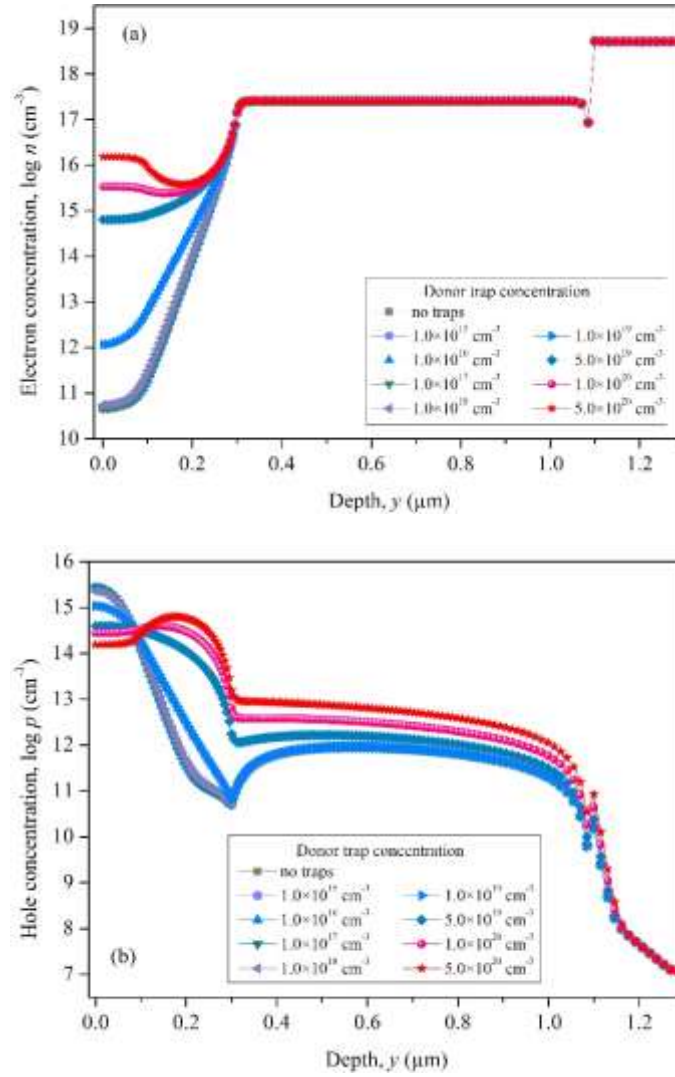


Fig. 12. Carrier concentration profiles along the device structure for different ET1 trap densities into the p^+ -region ($\lambda = 0.29 \mu\text{m}$). (a) Electrons. (b) Holes.

3.4.2 Acceptor trap HT1

In this section, we simulated the impact of an explicit acceptor trap density N_{ta} located into the n-region (HT1-type in Table 3). The detector SR behaviors assuming N_{ta} in the range $1 \times 10^{16} - 1 \times 10^{19} \text{ cm}^{-3}$ are shown in Fig. 13. Here, the wavelength range of the UV spectrum extends from $0.155 \mu\text{m}$ to $0.37 \mu\text{m}$.

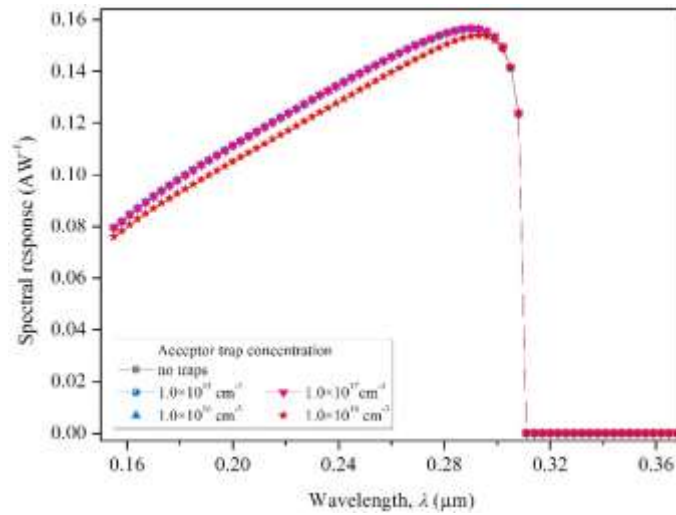
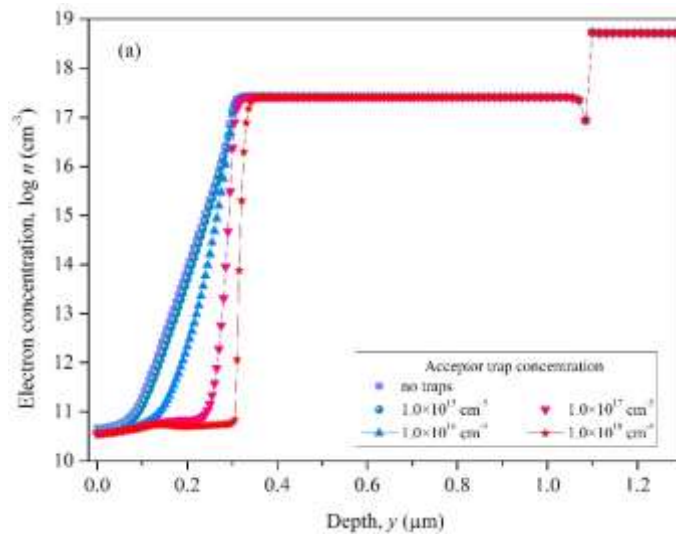


Fig. 13. SR for different concentrations of acceptor traps HT1 located into the n-region. The light intensity is 1 Wcm^{-2} at zero-bias voltage and $T = 300 \text{ K}$.

We can note that the HT1 traps have almost no impact on the detector SR for N_{ta} in the limit of $1 \times 10^{17} \text{ cm}^{-3}$. Then, however, only a limited SR decrease is observed for $N_{ta} = 1 \times 10^{18} \text{ cm}^{-3}$. The carrier concentration profiles along the device structure are shown in Fig. 14. They reveal in particular that the n-region ($0.1 < y < 0.4 \text{ μm}$) tends to be depleted of electrons as the trap concentration increases.



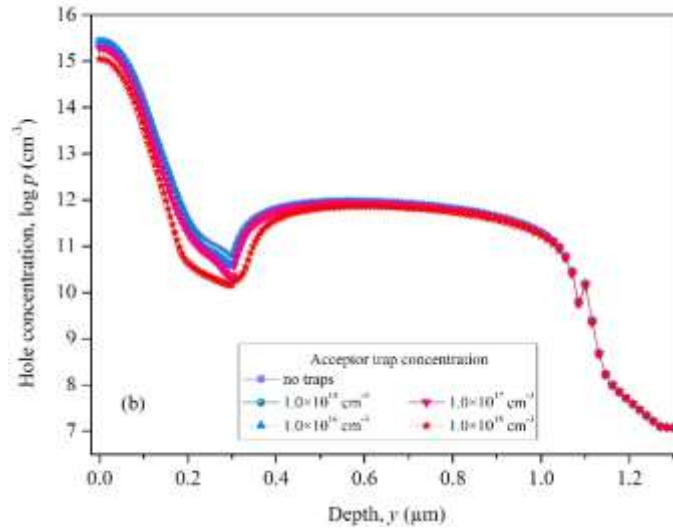
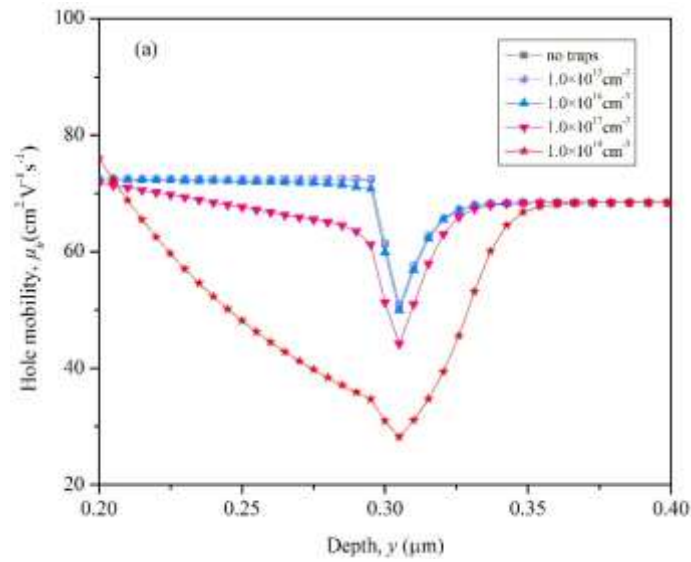


Fig. 14. Carrier concentration profiles along the device structure for different HT1 trap densities into the n-region ($\lambda = 0.29 \mu\text{m}$). (a) Electrons. (b) Holes.

Finally, it is worthwhile noting that the trap density increase is accompanied by a remarkable decrease in the carrier mobility behaviors into the device intrinsic region as shown in Fig. 15 for an ET1 and HT1 combined model.



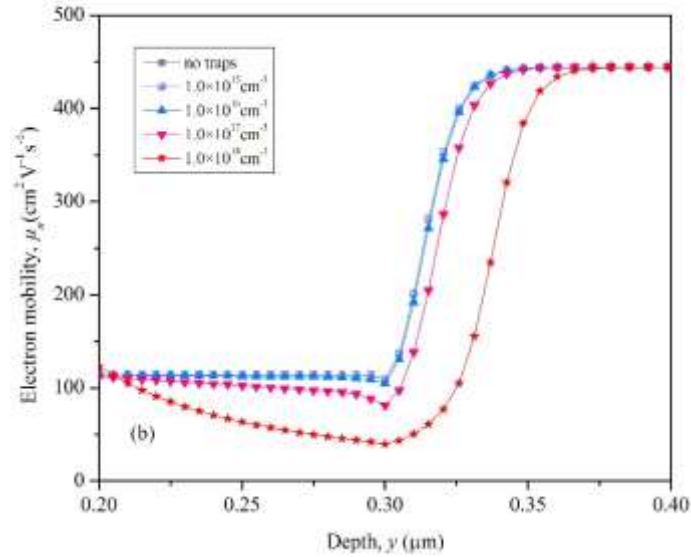


Fig. 15. Carrier mobility profiles along the device structure (intrinsic region) for different trap densities. (a) Holes. (b) Electrons.

4. Conclusion

In this paper, the performance of an optimized p^+n-n^+ $Al_{0.17}Ga_{0.83}N$ UV photodetector has been investigated. The fundamental geometrical and doping parameters have been carefully taken into account. The simulated $J(V)$ characteristics have shown that, in reverse bias conditions this structure is sensitive to the UV rays of different wavelengths and the shorter wavelengths generate the higher leakage currents. The detector SR can reach 0.156 AW^{-1} under a light intensity of 1 Wcm^{-2} at zero-bias voltage and room temperature. This peak value becomes close to 0.16 AW^{-1} for a reverse-bias voltage of -50 V . The detector cut-off wavelength is $0.31 \mu\text{m}$. The literature data of several devices based on the AlGaIn ternary compounds have been reported for comparison.

By increasing the temperature from 300 K to 500 K, a noticeable decrease in the SR behavior has been observed for temperatures exceeding 420 K. In particular, we have calculated a peak value limited to 0.141 AW^{-1} at $T = 500 \text{ K}$. The detector SR is also affected by an explicit trap concentration located into the p^+ and n regions. However, the SR curve gradually decreases only for acceptor and donor trap densities that are about three orders of magnitude higher than the local (total) doping concentration. These results seem to predict an apparent robustness of the proposed device structure.

References

- [1] G. Wang, K. Fu, C.S. Yao, D. Su, G.G. Zhang, J.Y. Wang, M. Lu, Nucl. Instrum. Methods Phys. Res., Sect. A 663, 10 (2012).
- [2] M.S.P. Reddy, A.A. Kumar, V.R. Reddy, Thin Solid Films 519, 3844 (2011).
- [3] F. Bouzid, L. Dehimi, F. Pezzimenti, Journal of Elec Materi (2017) 46: 6563.
- [4] F. Bouzid, F. Pezzimenti, L. Dehimi, M. L. Megherbi, F.G. Della Corte, Jpn. J. Appl. Phys. 56 094301(2017).

- [5] L.C. Chen, C.Y. Hsu, W.H. Lan, S.Y. Teng, *Solid-State Electron.* 47, 1843 (2003).
- [6] Y.K. Su, F.S. Juang, M.H. Chen, *Jpn. J. Appl. Phys.* 42, 2257 (2003).
- [7] R. Werner, M. Reinhardt, M. Emmerling, A. Forchel, V. Harle, A. Bazhenov, *Physica E* 7, 915 (2000).
- [8] Y.Q. Yu, L.B. Luo, M.Z. Wang, B. Wang, L.H. Zeng, C.Y. Wu, J.S. Jie, J.W. Liu, L. Wang, and S.H. Yu, *Nano Res.* 8, 1098 (2015).
- [9] J. Li, M. Zhao, X.F. Wang, *Phys. B* 405, 996 (2010).
- [10] E. Ozbay, N. Biyikli, I. Kimukin, T. Kartaloglu, T. Tut, O. Aytur, *IEEE J. Sel. Top. Quantum Electron.* 10, 742 (2004).
- [11] Q. Chen, J.W. Yang, A. Osinsky, S. Gangopadhyay, B. Lim, M.Z. Anwar, M. Asif Khan. *Appl. Phys. Lett.* 70, 2277 (1997).
- [12] P. Mulligan, J. Wang, L. Cao, *Nucl. Instrum. Methods A* 719, 13 (2013).
- [13] Q. Chen, M.A. Khan, C.J. Sun, J.W. Yang, *Electron. Lett.* 31, 1781 (1995).
- [14] G. Parish, S. Keller, P. Kozodoy, J.P. Ibbetson, H. Marchand, P.T. Fini, S.B. Fleischer, S.P. Den Baars, U.K. Mishra, E.J. Tarsa, *Appl. Phys. Lett.* 75, 247 (1999).
- [15] A. Hirano, C. Pernot, M. Iwaya, T. Detchprohm, H. Amano, I. Akasaki, *Phys. Status Solidi A* 188, 293 (2001).
- [16] E. Monroy, M. Hamilton, D. Walker, P. Kung, F.J. Sanchez, M. Razeghi, *Appl. Phys. Lett.* 74, 1171 (1999).
- [17] C.K. Wang, Y.Z. Chiou, S.J. Chang, W. Chih Lai, S.P. Chang, C.H. Yen, C.C. Hung, *IEEE Sens. J.* 15, 4743 (2015).
- [18] W. Jun, Z. Degang, L. Zongshun, F. Gan, Z. Jianjun, S. Xiaomin, Z. Baoshun, Y. Hui, *Sci. China Phys. Mech.* 46, 198 (2003).
- [19] D. Walker, E. Monroy, P. Kung, J. Wu, M. Hamilton, F.J. Sanchez, J. Diaz, M. Razeghi, *Appl. Phys. Lett.* 74, 762 (1999).
- [20] W. Yang, T. Nohova, S. Krishnankutty, R. Torreano, S. McPherson, H. Marsh, *Appl. Phys. Lett.* 73, 1086 (1998).
- [21] S.K. Zhang, W.B. Wang, I. Shtau, F. Yun, L. He, H. Morkoc, X. Zhou, M. Tamargo, R.R. Alfano, *Appl. Phys. Lett.* 81, 4862 (2002).
- [22] M.A. Khan, J.N. Kuznia, D.T. Olson, M. Blasingame, A.R. Bhattarai, *Appl. Phys. Lett.* 63, 2455 (1993).
- [23] A. Osinsky, S. Gangopadhyay, J.W. Yang, R. Gaska, D. Kuksenkov, H. Temkin, I.K. Shmagin, Y.C. Chang, J.F. Muth, R.M. Kolbas, *Appl. Phys. Lett.* 72, 551 (1998).
- [24] H. Jiang, T. Egawa, H. Ishikawa, C. Shao, T. Jimbo, *Jpn. J. Appl. Phys.* 43, L683-L685 (2004).
- [25] G. Parish, S. Keller, P. Kozodoy, J.P. Ibbetson, H. Marchand, P.T. Fini, S.B. Fleischer, S.P. Den Baars, U.K. Mishra, E.J. Tarsa, *Appl. Phys. Lett.* 75, 247–249 (1999).
- [26] C. Pernot, A. Hirano, M. Iwaya, T. Detchprohm, H. Amano, I. Akasaki, *Jpn. J. Appl. Phys.* 39, L387–L389 (2000).

- [27] E. J. Tarsa, P. Kozodoy, J. Ibbetson, B. P. Keller, *Appl. Phys. Lett.*, 77, 316-318 (2000).
- [28] D.J.H. Lambert, M.M. Wong, U. Chowdhury, C. Collins, T. Li, U.K. Kwon, B.S. Shelton, T.G. Zhu, J.C. Campbell, R.D. Dupuis, *Appl. Phys. Lett.* 77, 1900–1902 (2000).
- [29] M.M. Wong, U. Chowdhury, C.J. Collins, B. Yang, J.C. Denyszyn, K.S. Kim, J.C. Campbell, R.D. Dupuis, *Phys. Status Solidi A* 188, 333–336 (2001).
- [30] C.J. Collins, U. Chowdhury, M.M. Wong, B. Yang, A.L. Beck, R.D. Dupuis, J.C. Campbell, *Appl. Phys. Lett.* 80, 3754–3756 (2002).
- [31] M.B. Reine, A. Hairston, P. Lamarre, K.K. Wong, S.P. Tobin, A.K. Sood, C. Cooke, M. Pophristic, S. Guo, B. Perez, R. Singh, C.R. Eddy Jr. U. Chowdhury, M.M. Wong, R.D. Dupuis, T. Li, S.P. Den Baars, *SPIE Proc.* 6119, 6119011–61190115 (2006).
- [32] E. Cicek, R. McClintock, Z. Vashaei, Y. Zhang, S. Gautier, C.Y. Cho, M. Razeghi, *Appl. Phys. Lett.* 102, 051102 (2013).
- [33] L.E. Rodak, A.V. Sampath, C.S. Gallinat, Y. Chen, Q. Zhou, J.C. Campbell, H. Shen, M. Wraback, *Appl. Phys. Lett.* 103, 0711101–0711104 (2013).
- [34] E. Cicek, R. McClintock, A. Haddadi, W.A. Gaviria Rojas, M. Razeghi, *IEEE J. Quantum Electron.* 50, 593–597 (2014).
- [35] X.L. Zhou, M.H. Yang, J.F. Du, *J. Electron. Sci. Tech. China*, 7, 3 (2009).
- [36] Z. Mi, C. Jagadish, *III-Nitride Semiconductor Optoelectronics (Semiconductors and Semimetals) 1st Edition*, 96, Elsevier Inc., 2017.
- [37] H. Dakhlaoui, *J. Appl. Phys.*, 117, 1357051-1357059 (2015).
- [38] *Silvaco Atlas User's Manual, Device Simulator Software* (2013).
- [39] K.H. Kim, T.H. Lee, K.R. Son, T.G. Kim, *Mater Design*, 153, 94-103 (2018).
- [40] T. Jang, J.W. Erickson, L.M. Porter, *J. Electron. Mater.*, 31, 5 (2002).
- [41] M. Henini, M. Razeghi, *Optoelectronic Devices III Nitrides*, 1st Edition, ch. 10, Elsevier Science, 2005.
- [42] M. Kneissl, J. Rass, *III-Nitride Ultraviolet Emitters Technology and Applications*, ch. 9, Springer International Publishing, 2016.
- [43] Y. Marouf, L. Dehimi, F. Bouzid, F. Pezzimenti, F.G. Della Corte, *Optik*, 163, 22-32 (2018).
- [44] M.L. Megherbi, F. Pezzimenti, L. Dehimi, A. Saadoune, F.G. Della Corte, *J. Electron. Mater.* 47, 1414-1420 (2018).
- [45] F. Pezzimenti, L. F. Albanese, S. Bellone, F.G. Della Corte, *Proc. IEEE BCTM – Bipolar/BiCMOS Circuits and Technology Meeting*, 214-217 (2009).
- [46] F. Pezzimenti, F.G. Della Corte, *Proc. MELECON - Mediterranean Electrotechnical Conference*, 1129-1134 (2010).
- [47] G. De Martino, F. Pezzimenti, F.G. Della Corte, G. Adinolfi, G. Graditi, *Proc. PRIME - 13th Conference on PhD Research in Microelectronics and Electronics*, 221-224 (2017).
- [48] H. Morkoç, *Handbook of Nitrides Semiconductors and Devices*, Wiley, Weinheim, 2008.

[49] A.Y. Polyakov, I.H. Lee, Mater. Sci. Eng. R, 94, 1-56 (2015).

[50] T. Mattila, R.M. Nieminen, Phys. Rev. B 54, 16676 (1996).